



Examining diesel-spray assisted ignition of ammonia under reactivity-controlled conditions using large-eddy simulations

Pushan Sharma^{a,*}, Davy Brouzet^a, Wai Tong Chung^a, Matthias Ihme^{a,b}

^a Department of Mechanical Engineering, Stanford University, Stanford, CA 94305, USA

^b Department of Photon Science, SLAC National Accelerator Laboratory, Menlo Park, CA 94025, USA

ARTICLE INFO

Keywords:

Ammonia
Reactivity controlled compression ignition (RCCI)
Auto-ignition
Diffuse-interface method
Large eddy simulation
ECN spray A
Dual-fuel combustion

ABSTRACT

Ammonia (NH₃) has gained increasing attention as a promising carbon-free fuel for compression ignition engines. Nonetheless, its poor combustion characteristics and elevated nitrogen oxides (NO_x) emissions present substantial obstacles. In the present study, we examine the utility of incorporating NH₃ as a low-reactivity fuel (LRF) in diesel-assisted dual-fuel combustion under Reactivity Controlled Compression Ignition (RCCI) conditions. Three large-eddy simulations (LES) are performed to quantify the effect of varying concentrations of NH₃ as LRF on the ignition characteristics and flame structure. The computational setup corresponds to the Engine Combustion Network (ECN) Spray A configuration, which provides the baseline for the present analysis. The ignition of the dodecane spray is found to be delayed by the presence of NH₃, which increases with increasing NH₃ content in the ambient. Local flamelets are extracted to examine the evolution of the flame structure starting from ignition at richer mixtures through low-temperature chemistry of dodecane, to finally stabilizing at the stoichiometric conditions. Near ignition, NH₃ oxidation is observed to follow the autoignition behavior of the most reactive mixture fraction, whereas at post-ignition the behavior shifts towards canonical premixed flame propagation. This study shows that using NH₃ as LRF under RCCI conditions offers an effective solution for NH₃ operation in CI engines to reduce carbon emissions.

1. Introduction

Compression ignition (CI) diesel engines are often used in heavy-duty applications such as rail, marine, and trucks due to their outstanding reliability and thermal efficiency [1]. In the last decade, dual fuel (DF) combustion under reactivity-controlled compression ignition (RCCI) conditions has emerged as a promising technology to meet emission regulations. Indeed, RCCI reduces nitrogen oxides (NO_x) emissions through low temperature fuel-lean combustion [1,2]. In a DF engine, high-reactivity fuel (HRF), e.g., diesel, is injected into a lean mixture of low-reactivity fuel (LRF) and air. Autoignition of the HRF acts as an energy source to ignite the surrounding premixed LRF/air mixture. Typically the HRF is consumed by a mixing-controlled diffusion flame as in conventional CI engines, whereas the LRF is consumed through mixed combustion modes [3].

Another promising approach for reducing engine emissions involves carbon-free fuels such as ammonia (NH₃) [4–6]. Compared to other carbon-free fuels, NH₃ offers (i) renewable means of production via green hydrogen, derived from renewable energy sources and (ii) economical storage and transportation through existing liquid-fuel infrastructure [7]. However, NH₃ possesses unfavorable combustion behavior

such as low flame speed, relatively lower heating value, longer ignition delay time (IDT), and larger flame thickness compared to conventional hydrocarbon fuels, and its propensity to form nitrogen-containing pollutants including unburnt fuel, nitrogen oxides (NO_x) and nitrous oxide (N₂O) [8]. Several approaches have been investigated to address these undesirable properties, such as addition of hydrogen [9], using swirling injectors [10], porous media combustors [11], or utilizing high compression ratios [4,5].

While direct combustion of NH₃ is challenging, it has shown promise when used as LRF in DF engines. Through experiments, Reiter and Kong [12] showed that effective operation of a heavy-duty engine can be achieved when NH₃, constituting 95% of the total energy, is ignited by high-reactivity diesel fuel. Recently, Yousefi et al. [10,13] carried out RCCI experiments in a diesel-NH₃ DF engine, which suggested that NH₃ DF engines can attain comparable thermal efficiencies to single-fuel diesel engines with reduced greenhouse-gas (GHG) and NO_x emissions if injection timing was optimized. Another experimental study [14] showed that unburnt fuel emissions can be reduced through multiple HRF injections.

* Corresponding author.

E-mail address: ps729@stanford.edu (P. Sharma).

<https://doi.org/10.1016/j.proci.2024.105317>

Received 5 December 2023; Accepted 22 May 2024

Available online 28 June 2024

1540-7489/© 2024 The Combustion Institute. Published by Elsevier Inc. All rights are reserved, including those for text and data mining, AI training, and similar technologies.

Numerical simulations involving Reynolds-Averaged Navier–Stokes (RANS) and large eddy simulations (LES) can provide detailed insights on NH_3 DF combustion. Li et al. [7] investigated the effects of low- and high-pressure DF injection through RANS simulations of marine engines. This study showed that the proportion of fossil fuel-based HRF can be reduced with high-pressure injection, while low-pressure injection results in higher thermal efficiencies.

Several LES studies [15–17] have focused on variations of the engine combustion network (ECN) spray A configuration [18]. For RCCI configurations, previous works have focused on different fuels including methane [3,19,20], methane–hydrogen [21], and methane–methanol blends [22]. However, numerical studies of NH_3 under RCCI conditions remain largely limited to RANS studies [23,24].

Within these contexts, the objective of this work is to examine the effects of NH_3 on DF autoignition and flame structure with RCCI operating conditions. To this end, we perform LES of dodecane– NH_3 DF liquid-fuel combustion simulations under engine-like conditions using skeletal finite-rate chemistry and the diffusive-interface method. Section 2 provides the details of the governing equations and simulation set-up. Results, including detailed analyses of NH_3 combustion and flame structure, are presented in Section 3, followed by concluding remarks in Section 4.

2. Methodology

2.1. Mathematical model

For the current study, we employ a diffuse-interface method [25] to simulate DF combustion. This method has been applied to previous LES studies under trans- and supercritical conditions for ECN diesel configurations Spray A and Spray D [15–17]. At supercritical high-pressure conditions, there is no distinction between the vapor and the liquid boundary, which enables to thermodynamically model the flow as a single phase using a real-fluid equation of state, which is modeled in this work with the Peng–Robinson (PR) cubic equation of state. Takahashi's high-pressure correction [26] is used for binary diffusion coefficients. The dynamic viscosity and thermal conductivity are evaluated by employing the high pressure correction by Chung et al. [27].

A compressible unstructured finite-volume solver [15–17] is used to numerically solve Favre-filtered conservation laws for mass, momentum, total energy, and chemical species. The convective fluxes are discretized using a sensor-based hybrid scheme, enhanced by the entropy-stable flux correction method along with an adaptive double-flux method to eliminate spurious pressure oscillations when employing a fully conservative scheme [25]. We apply a second-order accurate simpler balanced-splitting scheme [28] to separate the convection, diffusion, and reaction operators. The stiff chemical source terms are integrated using a semi-implicit fourth order accurate Rosenbrock–Krylov scheme [28]. For all other non-stiff operators, we utilize a strong stability preserving third-order Runge–Kutta (SSP-RK3) scheme [29]. For modeling turbulent stresses, we employ the Vreman sub-grid scale (SGS) model [30]. The turbulence-chemistry interaction is modeled using the dynamic thickened-flame model [31], with a maximum thickening factor set to 4 in this particular study [16,17].

Recently, Xu et al. [32] developed a detailed chemical mechanism to model the chemical kinetics of dodecane– NH_3 mixtures. The mechanism involves 176 species and 2841 reactions, including a skeletal dodecane submechanism [33], a detailed ammonia submechanism [34], and the chemistry involving the interaction between $\text{C}_1/\text{C}_2\text{-NH}_3$ and NH_3 -Dodecane. The individual component of the detailed mechanism are validated for the thermodynamic condition that we are interested in this study. However, using such a detailed mechanism would be too expensive for the current study. Therefore, we used the AR-CANE [35] software based on direct relation graph with error propagation (DRGEP) [36] to generate a skeletal chemical model that involves

Table 1

Ambient compositions (mass fractions) of LRF00, LRF03 and LRF06 along with their Z_{st} , Z_{MR} , ϕ_{LRF} , first (τ_1) and second (τ_2) stage IDT and lift-off height. Note that LRF00 corresponds to ECN spray A composition.

Parameter	LRF00	LRF03	LRF06
O_2	0.228	0.217	0.208
CO_2	0.091	0.087	0.083
H_2O	0.022	0.021	0.020
N_2	0.659	0.628	0.601
NH_3	0.0	0.047	0.088
ϕ_{LRF}	0.0	0.3	0.6
Z_{st}	0.062	0.043	0.023
Z_{MR}	0.14	0.17	0.20
τ_1 [ms]	0.065	0.112	0.133
τ_2 [ms]	0.131	0.197	0.272
Lift-off height [mm]	10.51	13.36	16.25

the oxidation of dodecane– NH_3 mixtures, consisting of 75 species and 400 reactions. The reductions are performed based on 0D auto-ignition simulations at 60 bar pressure and a wide range of temperatures and equivalence ratios. Although the uncertainties of kinetic mechanisms for dodecane– NH_3 mechanisms remain high, the original detailed mechanism is the most comprehensive one that could be found and we performed a thorough validation of the reduced mechanism in terms of IDT and major species concentrations. More details about the chemical mechanism reduction and validation are provided as supplementary information.

2.2. Simulation configuration

This study considers the Spray A single-hole injector configuration, conforming to the standardized design for CI engine sprays from prior studies, as defined by the ECN benchmark [18]. Liquid n-dodecane ($\text{C}_{12}\text{H}_{26}$) fuel is injected at a sub-critical temperature of $T_{\text{inj}} = 363\text{K}$ into a chamber at an ambient condition of $p_\infty = 60\text{bar}$ and $T_\infty = 1000\text{K}$ at an injection pressure of 1500 bar. In the context of NH_3 -diesel combustion, the injection pressures in experimental studies of RCCI engines vary widely, from as low as 200 bar [37] to 1900 bar [38] depending on the operating conditions. Thus the spray A configuration for this study is considered to be representative for RCCI conditions. We perform three simulations with varying mass fractions of NH_3 in the ambient composition, emulating different equivalence ratios of LRF for RCCI operating conditions. In the first case, referred as 'LRF00' hereafter, the conditions correspond to the original ECN spray A configuration, which is used as baseline in the present study. In the second and third simulations, NH_3 is premixed with the ambient of LRF00 with an equivalence ratio of $\phi_{\text{LRF}} = 0.3$ ('LRF03') and 0.6 ('LRF06'). The detailed ambient compositions of these simulations are reported in Table 1.

The mixture fraction (Z) in this study uses Bilger's definition [40] including the elemental mass fractions of C, H, O and N elements: $Z = (\beta - \beta_{\text{amb}})/(\beta_{\text{F}} - \beta_{\text{amb}})$ where

$$\beta = 2 \frac{Y_{\text{C}}}{W_{\text{C}}} + \frac{1}{2} \frac{Y_{\text{H}}}{W_{\text{H}}} + \frac{3}{4} \frac{Y_{\text{N}}}{W_{\text{N}}} - \frac{Y_{\text{O}}}{W_{\text{O}}} \quad (1)$$

The subscript 'F' and 'amb' correspond to dodecane fuel stream and ambient, respectively, and Y_i and W_i are the mass fraction and atomic weight of the i th element. The stoichiometric mixture fractions (Z_{st}) for LRF00, LRF03 and LRF06 are provided in Table 1.

The 3D computational domain is cylindrical (40 mm in diameter and 80 mm in axial length) with a structured mesh adopted from previous studies [15–17]. The mesh convergence has also been examined in these prior studies along with the validation of the numerical setup with experimental data by comparing liquid and vapor penetration lengths and ignition delay times. The mesh contains 2.2 million hexahedral elements with a minimum grid spacing of 8 μm near the injector to resolve the ignition kernel accurately.

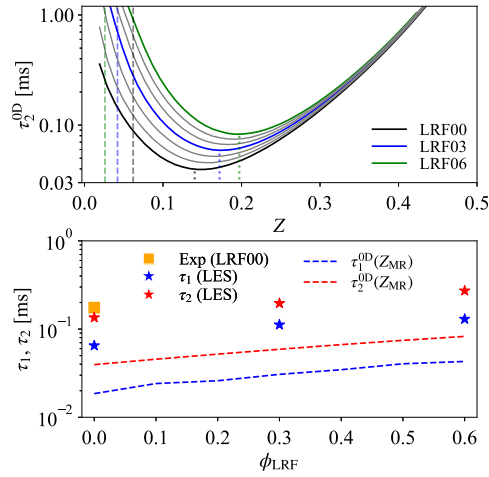


Fig. 1. Top: Homogeneous 0D reactor based IDT as a function of Z for different ϕ_{LRF} (gray lines). ϕ_{LRF} used in the LES are colored by black (LRF00: spray A), blue (LRF03) and green (LRF06). Minimum of each curve represents Z_{MR} (dotted line). The dashed lines correspond to Z_{st} of each case. Bottom: Computed values of IDT, τ_1 and τ_2 , for LRF00, LRF03 and LRF06. The experimental data is from Gehmlich et al. [39]. The dashed lines correspond to first and second stage IDT corresponding to Z_{MR} at different ϕ_{LRF} . (For interpretation of the references to color in this figure legend, the reader is referred to the web version of this article.)

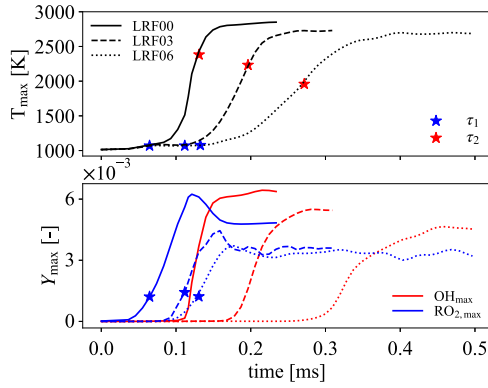


Fig. 2. Evolution of maximum temperature, OH and RO_2 mass fractions over the computational domain. (For interpretation of the references to color in this figure legend, the reader is referred to the web version of this article.)

3. Results and discussion

3.1. Effect of NH_3 on IDT

Analyzing the ignition delay time through calculations in homogeneous systems provides valuable understanding of the autoignition process. In this context, IDT of homogeneous dodecane/ambient mixtures are performed first, with the oxidizer being the ambient mixture with an equivalence ratio of ϕ_{LRF} . The initial compositions and temperature are computed based on the adiabatic mixing line of dodecane and the ambient. Following [19], we define the first stage IDT (τ_1 , \star) in both 0D and LES as the time when the dodecyl peroxy radical $C_{12}H_{25}O_2$ (RO_2) mass fraction reaches 20% of its maximum value in the LRF00 case. The second stage IDT (τ_2 , \star) is defined based on the maximum temperature gradient [17]. The second stage IDT (τ_2) from 0D calculations as a function of Z is shown in Fig. 1(top) for LRF00, LRF03 and LRF06. The minimum of each curve corresponds to the most reactive mixture fraction, Z_{MR} . The Z_{MR} values for all three cases are provided in Table 1. The autoignition in diffusion-controlled flames occurs somewhere along the Z_{MR} isoline, where the mixture fraction gradient or the scalar dissipation rate is low [41]. For the DF

mixture, increasing ϕ_{LRF} increases the IDT, and shifts Z_{MR} to richer mixtures. The lift-off height for all three cases are also provided in Table 1. In accordance with ECN recommendations, the lift-off length is described as the minimum axial distance from the injection location to the location where 2% of the maximum OH mass fraction is observed. For LRF00, we observe a lift-off height of 10.51 mm, demonstrating good agreement with experimental results of Gehmlich et al. [39], where a 10 mm lift-off height is reported. Furthermore, the flame lift-off height increases with increasing NH_3 content in the ambient.

Fig. 1(bottom) shows the IDT predictions from LES as a function of ϕ_{LRF} and compares the second stage IDT of the LRF00 case (spray A) with experimental data [39] for further validation. The LES underpredicts IDT for the spray A baseline case by approximately 20%, which is similar to prior observations [16,17]. This panel also includes the variation of IDT from homogeneous reactor calculations as a function of ϕ_{LRF} at their corresponding Z_{MR} . Because 3D effects such as turbulent mixing and scalar dissipation rates delay the ignition process [41], the IDTs obtained from the LES are appreciably higher than their 0D counterparts. However, the ratio between LES and 0D IDTs are found to be nearly constant, with values between 3.1 and 3.6. These findings suggest that 0D reactors could be used to estimate IDT in 3D RCCI configurations with NH_3 , consistent with ignition studies for other fuels [20,41].

Fig. 2 shows the temporal evolution of maximum values of temperature (T_{max}), RO_2 and OH mass fractions for all three cases as markers for low-temperature combustion (LTC) and high temperature combustion (HTC) [19]. The impact of an increasing amount of NH_3 on ignition and the evolution of temperature and mass fractions are evident in Fig. 2. The first stage IDT for LRF03 and LRF06 are 0.112 and 0.133 ms, which are approximately 1.7 and 2 times longer, respectively, compared to LRF00 (Table 1). This delayed LTC activation can be attributed to lower concentrations of RO_2 compared to LRF00. In particular, LTC initiation typically involves the production of RO_2 through H-abstraction of dodecane [32]. However, the presence of NH_3 introduces competition for OH radicals through NH_3 decomposition via $NH_3 + OH \rightleftharpoons NH_2 + H_2O$, consequently suppressing the LTC chain-branching pathways of dodecane [32]. As a result, not only the first stage IDT is delayed, but also the overall maximum RO_2 mass fraction decreases with increasing NH_3 . Following LTC, each case evolves towards high-temperature second stage ignition, during which both maximum temperature and OH mass fraction increase rapidly. The inhibition effect of NH_3 is also prominent in the second stage ignition as the slope of the temperature rise decreases considerably with NH_3 addition. This results in a second stage IDT of 0.191 and 0.272 ms for LRF03 and LRF06, respectively. The observations from 0D calculations (Fig. 1), exhibit a similar delay in the first and second stage ignition in the presence of NH_3 .

3.2. Combustion modes and flamelet topology

Fig. 3 shows the instantaneous flowfields of temperature, mixture fraction and an NH_3 progress variable Λ_{NH_3} at the center plane at the specific time instant $1.5\tau_2$. We define the NH_3 progress variable as $\Lambda_{NH_3} = 1 - (Y_{NH_3}/Y_{NH_3}^u(Z))$ where $Y_{NH_3}^u(Z)$ is the mass fraction of unburnt NH_3 on the mixing line; $\Lambda_{NH_3} = 0$ corresponds to unburnt NH_3 and $\Lambda_{NH_3} = 1$ correspond to fully consumed NH_3 , respectively. We also define another progress variable (C) based on dodecane oxidation products $C = 1 - (\sum_k Y_k / \sum_k Y_k^u(Z))$, where $k = \{CO, CO_2, H_2O, H_2\}$.

Fig. 3 first row exhibits distinct combustion modes, including LTC, HTC, and non-premixed combustion, characterized using criteria similar to Dalakoti et al. [42]. Specifically, LTC regions are identified below a critical temperature, $T_{crit} = 1120$ K, and above a critical RO_2 mass fraction (5% of $Y_{RO_2}^{max}$). HTC regions are classified when the temperature surpasses T_{crit} , and the OH mass fraction falls below a critical threshold (5% of Y_{OH}^{max}). HTC regions are further categorized into endothermic and exothermic segments based on the sign of the heat release rate (HRR). Regions where both temperature and OH mass fraction exceed

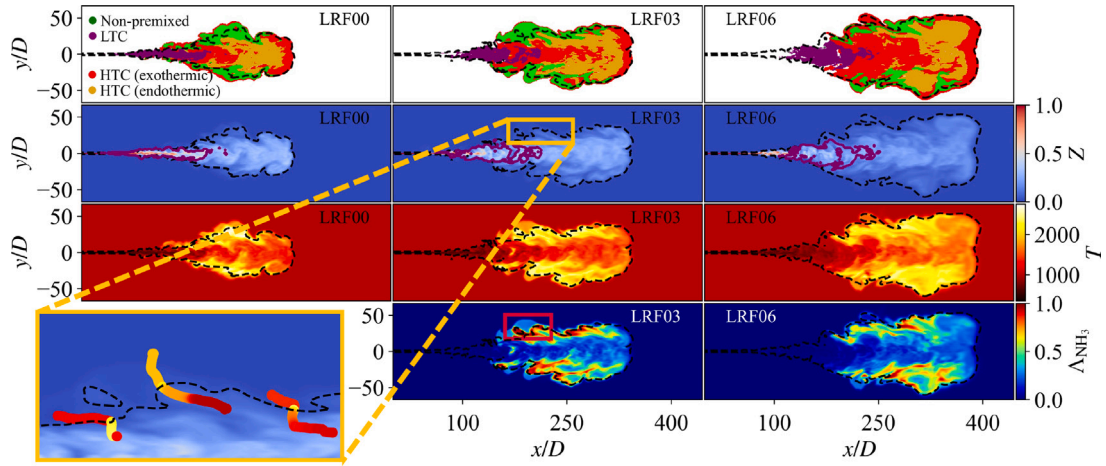


Fig. 3. Instantaneous flowfields for three cases considered; First row shows different combustion regimes, Second to fourth row depict instantaneous flowfields of mixture fraction, temperature and the progress variable of ammonia (Λ_{NH_3}), respectively. Three columns from left to right correspond to LRF00, LRF03 and LRF06, respectively. The boundary of the LTC region (purple) is superimposed on the mixture fraction field. An inset of the mixture fraction flowfield for LRF03 is shown in first column of fourth row, which shows a few extracted flamelets colored by temperature. D is the jet diameter. (For interpretation of the references to color in this figure legend, the reader is referred to the web version of this article.)

critical values are designated as the non-premixed mode of combustion. The mode analysis encompasses all states within flames where $|\text{HRR}| > 5 \times 10^9 \text{ W/m}^3$.

The initiation of LTC combustion for dodecane and the formation of RO_2 is observed to shift further downstream in the axial direction with the introduction of NH_3 as can be seen from the combustion mode analysis in the first row of Fig. 3. For LRF03 and LRF06, this shift extends the flame lift-off position, as shown in Table 1. A higher lift-off facilitates a longer mixing time and a more diluted dodecane core, as evident from the mixture fraction flowfields (second row of Fig. 3). For the LRF00 case (baseline spray A), the LTC region (purple boundary on Z contours) is more confined towards a fuel-rich region (higher Z), whereas the LRF03 and LRF06 LTC regions significantly lean out. As a result, we observe (1) a wider LTC distribution leaning more towards the ambient with increasing NH_3 , and (2) a reduced maximum temperature, OH mass fraction and HRR, which is consistent with the observations in Fig. 2. The HTC region exists further downstream of LTC, where temperature (third row of Fig. 3) is higher than the LTC region, increasing the NH_3 consumption (fourth row of Fig. 3) as well. The maximum temperature for all cases are observed near the stoichiometric mixture fraction, where NH_3 is fully consumed ($\Lambda_{\text{NH}_3} = 1$).

In Fig. 3, we have divided the HTC region in two parts based on its exo- or endothermicity. A substantial endothermic HTC region is evident for all three conditions. Despite the considerably high temperature in this region, subsequent to the premixed exothermic HTC region, the oxygen mass fraction approaches zero, reducing the overall reaction rates and resulting in negative HRR. NH_3 species consumption rate ($\dot{\omega}_{\text{NH}_3}$) approaches zero in these regions, resulting in 30%–50% unburnt NH_3 within the flame compared to ambient, as shown in Fig. 3.

The flowfields help to understand the combustion modes and flame structure spatially. Additionally, our objective is to investigate the temporal evolution of the flame structure and how it is affected by the varying concentrations of NH_3 , especially around the second stage ignition at τ_2 . We extract local flamelets from the simulations. This is achieved by computing the local mixture fraction gradient, $\nabla \tilde{Z}$, and integrating $d\mathbf{x} = \hat{n} d\tilde{Z}/|\nabla \tilde{Z}|$, where $\hat{n} = \nabla \tilde{Z}/|\nabla \tilde{Z}|$ [43]. This maps the mixture fraction space to physical space (\mathbf{x}). Starting from a flamelet at a pre-ignition time instant of $0.7\tau_2$, flamelets are tracked over time assuming a constant characteristics velocity that corresponds to the evolution of the vapor penetration rate [16]. A few examples of extracted flamelets are shown as an inset on the mixture fraction flowfield of LRF03 in Fig. 3. Evolution of different quantities, such

as temperature, OH and NO mass fractions, C and Λ_{NH_3} along the flamelets are compared in Fig. 4.

The following observations can be made for all three conditions. At $0.7\tau_2$, the flamelet structure is mostly controlled by the mixing process. Consequently, the consumption of NH_3 , C and other mass fractions are small. The flame ignites at a richer region than Z_{st} , corresponding to the most reactive mixture fraction (Z_{MR}) being richer than Z_{st} (Fig. 1). Consequently, we observe that the temperature profile along with C differ from the mixing profile. Their corresponding peaks persist in the richer region during subsequent time instants leading to the ignition time τ_2 , gradually shifting towards a leaner mixture. NO mass fraction increases in the fuel rich region at an intermediate temperature, which are typical conditions for activating the prompt NO_x pathways [32]. Progressing further in time, the maximum temperature eventually coincides with the stoichiometric mixture fraction, establishing a non-premixed mode of combustion (first row of Fig. 3). As expected, the peak temperature and maximum OH mass fractions are observed near Z_{st} , along with the maximum C and HRR (not shown here). As the temperature increases with time, the NO mass fraction also reaches its maximum at Z_{st} in both LRF03 and LRF06, which can be attributed to the thermal NO_x pathways [32]. The previous peak of NO mass fractions persists in the fuel-rich region, which indicates that the prompt NO production remains active in these regions.

For the RCCI cases with NH_3 as LRF, the evolution of Λ_{NH_3} closely follows the evolution of temperature and OH mass fraction, especially at $Z > Z_{\text{st}}$, which shows that the NH_3 combustion in the rich region is controlled by the oxidation of the primary fuel. However, on the leaner side, a peak in temperature and Λ_{NH_3} is clearly visible for LRF03 case around τ_2 . We should emphasize that at τ_2 , the primary reacting profile discussed above falls in the richer region approaching the equilibrium solution at Z_{st} . This indicates combustion of NH_3 at an early stage near τ_2 at $Z < Z_{\text{st}}$. The subsequent section will examine in more details whether this phenomenon is the auto-ignition of NH_3 or not. Eventually, as the flamelet reaches its equilibrium solution, the peaks merge, and NH_3 is fully consumed at $Z = Z_{\text{st}}$. The overall evolution of Λ_{NH_3} is similar for both LRF03 and LRF06. However, the inhibiting effect of adding NH_3 reduces the maximum temperature and OH mass fractions. The flamelet analysis in the third column of Fig. 4 suggests LRF06 to be less prone to producing NO than LRF03. This finding may not be accurate as the timescales for the formation of NO_x is typically longer compared to other species. Given the focus on dual-fuel ignition in this study, simulations were not run long enough to quantify the amount of NO_x resulting from the NH_3 combustion. However, it is evident that the NO_x production rate is significantly higher for LRF03 and LRF06 than its LRF00 counterpart.

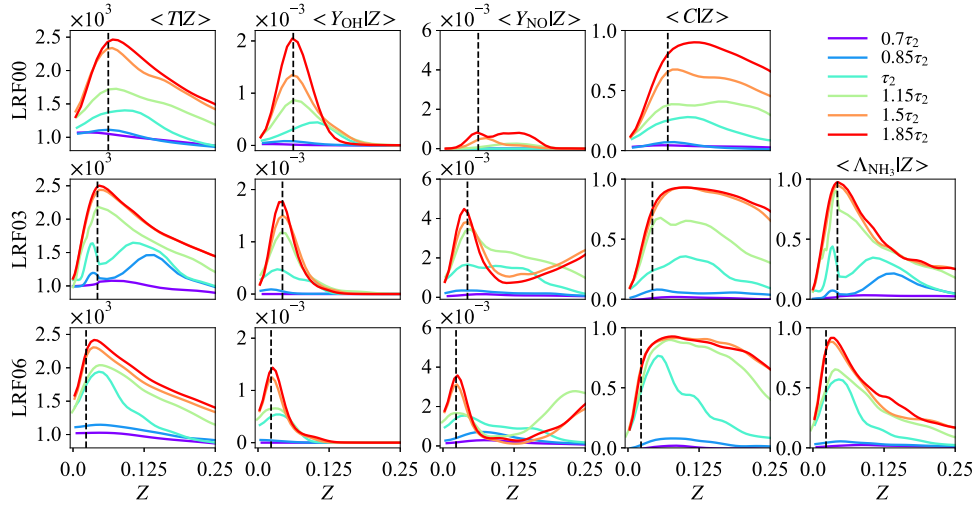


Fig. 4. Evolution of the flamelet topology. The first, second and third row correspond to the conditional means of temperature, Y_{OH} , Y_{NO} , C and A_{NH_3} for LRF00, LRF03 and LRF06, respectively. The vertical dashed line corresponds to Z_{st} . (For interpretation of the references to color in this figure legend, the reader is referred to the web version of this article.)

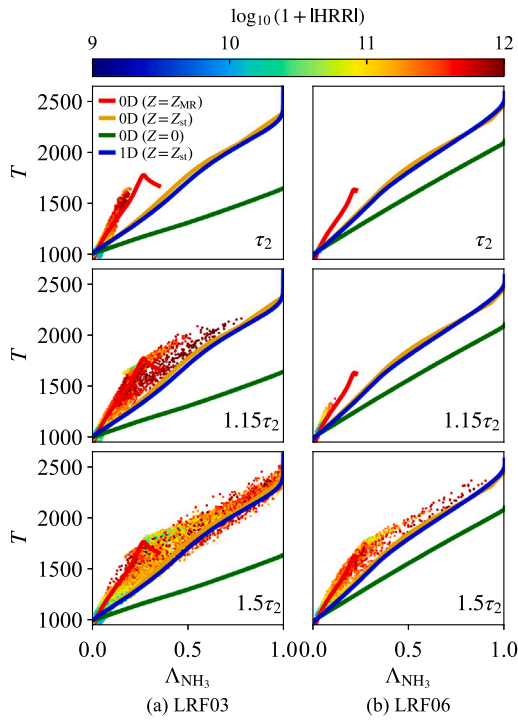


Fig. 5. Scatter plots of temperature as a function of A_{NH_3} at $Z < Z_{st}$ at three different time instants of LRF03 (first column) and LRF06 (second column). The red, orange, blue and green lines correspond to the homogeneous reactor (0D) simulation of $Z = Z_{MR}$, $Z = Z_{st}$, $Z = 0$ (ambient NH_3) mixtures, and 1D laminar premixed flame simulation of $Z = Z_{st}$ mixture. (For interpretation of the references to color in this figure legend, the reader is referred to the web version of this article.)

3.3. NH_3 flame initiation and propagation

The previous discussion suggested early NH_3 combustion resulting in temperature rise at the leaner side of Z_{st} around the ignition (τ_2) in Fig. 4 for LRF03. Eventually, the observed peak in temperature and A_{NH_3} merges with the flame at Z_{st} as the flame evolves. In order to understand the initiation and propagation of NH_3 combustion, we focus on the compositions at $Z < Z_{st}$ in this analysis. Fig. 5 shows the compositions as a function of temperature and A_{NH_3} , at three different

time instants for LRF03 and LRF06, colored by HRR. We compare the evolution of temperature with homogeneous reactor calculations corresponding to mixtures $Z = Z_{MR}$, where the dodecane/ NH_3 flame is expected to ignite, the stoichiometric mixture corresponding to $Z = Z_{st}$, and $Z = 0$, which is the ambient NH_3 /air mixture with ϕ_{LRF} . We also evaluate an 1D unstrained premixed flame corresponding to the mixture of $Z = Z_{st}$. The compositions from 0D reactor and 1D premixed calculations corresponding to Z_{st} follow the same trend.

At τ_2 , the evolution of temperature in the LES closely follows the behavior of a homogeneous reactor corresponding to Z_{MR} (red line in Fig. 5). This suggests that the DF mixture ignites at Z_{MR} , and as both fuels are being consumed, temperature increases according to the red line. The HRR at the initial time instant is also high as it follows the conditions of Z_{MR} . However, the 0D reactor for Z_{MR} reaches its equilibrium temperature of approximately 1800 K, where dodecane is fully consumed leaving unburnt NH_3 at high temperatures. Similarly, the states from LES near the equilibrium temperature of 0D of Z_{MR} exhibits a decrease in HRR over time. These clusters appear as small pockets of unburnt NH_3 at a relatively high temperature between the flame at Z_{st} and the ambient. One such pocket of unburnt NH_3 is marked by a pink box on the A_{NH_3} contour plot in Fig. 3 for LRF03. At $1.15\tau_2$, as the flame evolves towards Z_{st} (Fig. 4), the temperature evolution in Fig. 5 also starts to shift towards the 1D premixed flame with stoichiometric mixture. At the final time step, we observe that all states are bounded by the 0D evolution of Z_{MR} and 1D calculations of Z_{st} . In Fig. 5, $A_{NH_3} = 1$ occurs at the flame location of $Z = Z_{st}$, where NH_3 is fully consumed. Compared to LRF03, the evolution of the composition is slower in LRF06, but they still follow the same trend as for LRF03.

The green line in all three plots corresponds to autoignition of ambient NH_3 mixture. The evolution of the scatter plots suggest that the ambient NH_3 does not auto-ignite throughout the simulation. Previous studies with methane as LRF [3] exhibited two different modes of LRF combustion, including autoignition. However, NH_3 consumption is dictated either by the auto-ignition of dodecane/ NH_3 fuel mixture, or the flame established at Z_{st} .

4. Conclusions

In this work, dodecane-assisted dual-fuel combustion of NH_3 under RCCI conditions is numerically investigated using LES in conjunction with a diffuse-interface method and finite-rate chemistry. The ECN spray A configuration is used as the baseline, which is modified to

study dual fuel combustion using different levels of NH_3 in the ambient mixture. The ignition characteristics in OD homogeneous reactor and 3D LES, and the evolution of the flame structure are investigated by varying the amount of NH_3 in the ambient. The results show the inhibiting effect of NH_3 on auto-ignition of dodecane as the IDT increases with increasing amount of NH_3 in the ambient.

Flamelets were extracted to investigate the evolution of the flame structure and different combustion modes of dodecane/ NH_3 mixture. This flamelet analysis revealed that NH_3 combustion is initiated by the activation of LTC of dodecane, which is then followed into HTC and finally NH_3 is consumed as the flame evolves towards stoichiometric condition at Z_{st} . However, at fuel-lean condition ($Z < Z_{\text{st}}$), NH_3 did not exhibit any autoignitive behavior. The evolution of the compositions in NH_3 progress variable space was observed to be bounded by OD homogeneous reactor and 1D premixed flame compositions of the Z_{MR} and Z_{st} , respectively. In summary, this study provides a fundamental analysis of NH_3 combustion under RCCI conditions, which shows a promising path for NH_3 utilization.

Novelty and Significance Statement

This research investigates ammonia combustion focusing on the fundamental aspects of diesel spray-assisted combustion using ammonia under a novel combustion mode linked to Reactivity Controlled Compression Ignition (RCCI). While recent experimental and numerical studies have primarily focused on global parameters such as emissions and engine efficiency for ammonia in CI engines, the present study provides detailed insight into the fundamental mechanisms in which a novel combustion mode enables stable ammonia combustion at reduced emissions. Specifically, we examine ignition characteristics, flame structure evolution, and various modes of ammonia combustion within the context of a 3D transcritical large eddy simulations with a diffuse-interface method and finite-rate chemistry. Our key findings suggest that (i) the presence of ammonia inhibits dodecane ignition, and (ii) the importance of dodecane low-temperature combustion in initiating ammonia combustion. These insights contribute significantly to understanding the potential of ammonia as a fossil-fuel replacement in compressionignition engine application.

CRedit authorship contribution statement

Pushan Sharma: Designed research, Analyzed data, Wrote the paper. **Davy Brouzet:** Designed research, Analyzed data, Revised paper. **Wai Tong Chung:** Performed simulations, Revised paper. **Matthias Ihme:** Designed research, Analyzed data, Revised paper.

Declaration of competing interest

The authors declare that they have no known competing financial interests or personal relationships that could have appeared to influence the work reported in this paper.

Acknowledgments

This work was supported by the Department of Energy Office of Energy Efficiency Renewable Energy (EERE) with award number DE-EE0008875 and by the Department of Energy National Nuclear Security Administration's Predictive Science Academic Alliance Program (PSAAP).

Appendix A. Supplementary material

Supplementary material related to this article can be found online at <https://doi.org/10.1016/j.proci.2024.105317>.

References

- [1] R.D. Reitz, G. Duraisamy, Review of high efficiency and clean reactivity controlled compression ignition (RCCI) combustion in internal combustion engines, *Prog. Energ. Combust. Sci.* 46 (2015) 12–71.
- [2] S.L. Kokjohn, R.M. Hanson, D. Splitter, R. Reitz, Fuel reactivity controlled compression ignition (RCCI): a pathway to controlled high-efficiency clean combustion, *Int. J. Engine Res.* 12 (3) (2011) 209–226.
- [3] M. Gadalla, S. Karimkashi, I. Kabil, O. Kaario, T. Lu, V. Vuorinen, Embedded direct numerical simulation of ignition kernel evolution and flame initiation in dual-fuel spray assisted combustion, *Combust. Flame* 259 (2024) 113172.
- [4] M.-C. Chiong, C.T. Chong, J.-H. Ng, S. Mashruk, W.W.F. Chong, N.A. Samiran, G.R. Mong, A. Valera-Medina, Advancements of combustion technologies in the ammonia-fuelled engines, *Energy Convers. Manage.* 244 (2021) 114460.
- [5] P. Dimitriou, R. Javadi, A review of ammonia as a compression ignition engine fuel, *Int. J. Hydrog. Energy* 45 (11) (2020) 7098–7118.
- [6] S. Manigandan, J.I. Ryu, T.P. Kumar, M. Elgendi, Hydrogen and ammonia as a primary fuel – A critical review of production technologies, diesel engine applications, and challenges, *Fuel* 352 (2023) 129100.
- [7] T. Li, X. Zhou, N. Wang, X. Wang, R. Chen, S. Li, P. Yi, A comparison between low-and high-pressure injection dual-fuel modes of diesel-pilot-ignition ammonia combustion engines, *J. Energy Inst.* 102 (2022) 362–373.
- [8] A. Valera-Medina, F. Amer-Hatem, A. Azad, I. Dedoussi, M. De Joannon, R. Fernandes, P. Glarborg, H. Hashemi, X. He, S. Mashruk, et al., Review on ammonia as a potential fuel: from synthesis to economics, *Energy Fuel* 35 (9) (2021) 6964–7029.
- [9] A.A. Khateeb, T.F. Guiberti, X. Zhu, M. Younes, A. Jamal, W.L. Roberts, Stability limits and NO emissions of technically-premixed ammonia-hydrogen-nitrogen-air swirl flames, *Int. J. Hydrog. Energy* 45 (41) (2020) 22008–22018.
- [10] A. Yousefi, H. Guo, S. Dev, B. Liko, S. Lafrance, Effects of ammonia energy fraction and diesel injection timing on combustion and emissions of an ammonia/diesel dual-fuel engine, *Fuel* 314 (2022) 122723.
- [11] G. Vignat, B. Akoush, E.R. Toro, E. Boigné, M. Ihme, Combustion of lean ammonia-hydrogen fuel blends in a porous media burner, *Proc. Combust. Inst.* 39 (4) (2023) 4195–4204.
- [12] A.J. Reiter, S.-C. Kong, Combustion and emissions characteristics of compression-ignition engine using dual ammonia-diesel fuel, *Fuel* 90 (1) (2011) 87–97.
- [13] A. Yousefi, H. Guo, S. Dev, S. Lafrance, B. Liko, A study on split diesel injection on thermal efficiency and emissions of an ammonia/diesel dual-fuel engine, *Fuel* 316 (2022) 123412.
- [14] Y. Niki, Y. Nitta, H. Sekiguchi, K. Hirata, Diesel fuel multiple injection effects on emission characteristics of diesel engine mixed ammonia gas into intake air, *J. Eng. Gas Turbines Power* 141 (6) (2019) 061020.
- [15] P.C. Ma, H. Wu, T. Jaravel, L. Bravo, M. Ihme, Large-eddy simulations of transcritical injection and auto-ignition using diffuse-interface method and finite-rate chemistry, *Proc. Combust. Inst.* 37 (3) (2019) 3303–3310.
- [16] W.T. Chung, P.C. Ma, M. Ihme, Examination of diesel spray combustion in supercritical ambient fluid using large-eddy simulations, *Int. J. Engine Res.* 21 (1) (2020) 122–133.
- [17] J. Guo, D. Brouzet, W.T. Chung, M. Ihme, Analysis of ducted fuel injection at high-pressure transcritical conditions using large-eddy simulations, *Int. J. Engine Res.* (2023) 14680874231170659.
- [18] L. Pickett, G. Bruneaux, R. Payri, Engine combustion network special issue, *Int. J. Engine Res.* 21 (1) (2020) 11–14.
- [19] H. Kahila, O. Kaario, Z. Ahmad, M.G. Masouleh, B. Tekgül, M. Larmi, V. Vuorinen, A large-eddy simulation study on the influence of diesel pilot spray quantity on methane-air flame initiation, *Combust. Flame* 206 (2019) 506–521.
- [20] B. Tekgül, H. Kahila, O. Kaario, V. Vuorinen, Large-eddy simulation of dual-fuel spray ignition at different ambient temperatures, *Combust. Flame* 215 (2020) 51–65.
- [21] J. Kannan, M. Gadalla, B. Tekgül, S. Karimkashi, O. Kaario, V. Vuorinen, Large-eddy simulation of tri-fuel ignition: diesel spray-assisted ignition of lean hydrogen-methane-air mixtures, *Combust. Theor. Model.* 25 (3) (2021) 436–459.
- [22] M. Gadalla, J. Kannan, B. Tekgül, S. Karimkashi, O. Kaario, V. Vuorinen, Large-eddy simulation of tri-fuel combustion: Diesel spray assisted ignition of methanol-hydrogen blends, *Int. J. Hydrogen. Energy* 46 (41) (2021) 21687–21703.
- [23] S. Frankl, S. Gleis, S. Karmann, M. Prager, G. Wachtmeister, Investigation of ammonia and hydrogen as CO_2 -free fuels for heavy duty engines using a high pressure dual fuel combustion process, *Int. J. Engine Res.* 22 (10) (2021) 3196–3208.
- [24] L. Xu, X.-S. Bai, Numerical investigation of engine performance and emission characteristics of an ammonia/hydrogen/n-heptane engine under RCCI operating conditions, *Flow. Turbul. Combust.* (2023) 1–18.
- [25] P.C. Ma, Y. Lv, M. Ihme, An entropy-stable hybrid scheme for simulations of transcritical real-fluid flows, *J. Comput. Phys.* 340 (2017) 330–357.
- [26] S. Takahashi, Preparation of a generalized chart for the diffusion coefficients of gases at high pressures, *J. Chem. Eng. Jpn.* 7 (6) (1975) 417–420.

- [27] T.H. Chung, M. Ajlan, L.L. Lee, K.E. Starling, Generalized multiparameter correlation for nonpolar and polar fluid transport properties, *Ind. Eng. Chem. Res.* 27 (4) (1988) 671–679.
- [28] H. Wu, P.C. Ma, M. Ihme, Efficient time-stepping techniques for simulating turbulent reactive flows with stiff chemistry, *Comput. Phys. Comm.* 243 (2019) 81–96.
- [29] S. Gottlieb, C.-W. Shu, E. Tadmor, Strong stability-preserving high-order time discretization methods, *SIAM Rev.* 43 (1) (2001) 89–112.
- [30] A. Vreman, An eddy-viscosity subgrid-scale model for turbulent shear flow: Algebraic theory and applications, *Phys. Fluids* 16 (10) (2004) 3670–3681.
- [31] O. Colin, F. Ducros, D. Veynante, T. Poinso, A thickened flame model for large eddy simulations of turbulent premixed combustion, *Phys. Fluids* 12 (7) (2000) 1843–1863.
- [32] S. Xu, G. Li, M. Zhou, W. Yu, Z. Zhang, D. Hou, F. Yu, Experimental and kinetic studies of extinction limits of counterflow cool and hot diffusion flames of ammonia/n-dodecane, *Combust. Flame* 245 (2022) 112316.
- [33] A. Stagni, A. Cuoci, A. Frassoldati, T. Faravelli, E. Ranzi, Lumping and reduction of detailed kinetic schemes: an effective coupling, *Ind. Eng. Chem. Res.* 53 (22) (2014) 9004–9016.
- [34] A. Stagni, C. Cavallotti, S. Arunthanayothin, Y. Song, O. Herbinet, F. Battin-Leclerc, T. Faravelli, An experimental, theoretical and kinetic-modeling study of the gas-phase oxidation of ammonia, *React. Chem. Eng.* 5 (4) (2020) 696–711.
- [35] Q. Cazères, P. Pepiot, E. Riber, B. Cuenot, A fully automatic procedure for the analytical reduction of chemical kinetics mechanisms for computational fluid dynamics applications, *Fuel* 303 (2021) 121247.
- [36] P. Pepiot-Desjardins, H. Pitsch, An efficient error-propagation-based reduction method for large chemical kinetic mechanisms, *Combust. Flame* 154 (1–2) (2008) 67–81.
- [37] C.M. Rousselle, P. Brequigny, A. Dupuy, Impact of splitting n-dodecane pilot injection on ammonia RCCI engine, *SAE Tech. Pap.* (2023).
- [38] L. Xu, S. Xu, X.-S. Bai, J.A. Repo, S. Hautala, J. Hyvönen, Performance and emission characteristics of an ammonia/diesel dual-fuel marine engine, *Renew. Sust. Energ. Rev.* 185 (2023) 113631.
- [39] R. Gehmlich, C. Mueller, D. Ruth, C. Nilsen, S. Skeen, J. Manin, Using ducted fuel injection to attenuate or prevent soot formation in mixing-controlled combustion strategies for engine applications, *Appl. Energy* 226 (2018) 1169–1186.
- [40] R. Bilger, The structure of turbulent nonpremixed flames, in: *Sym. Int. Combust. Combustion*, Vol. 22, No. 1, Elsevier, 1989, pp. 475–488.
- [41] E. Mastorakos, Ignition of turbulent non-premixed flames, *Prog. Energy. Combust. Sci.* 35 (1) (2009) 57–97.
- [42] D.K. Dalakoti, B. Savard, E.R. Hawkes, A. Wehrfritz, H. Wang, M.S. Day, J.B. Bell, Direct numerical simulation of a spatially developing n-dodecane jet flame under Spray A thermochemical conditions: Flame structure and stabilisation mechanism, *Combust. Flame* 217 (2020) 57–76.
- [43] W.L. Chan, H. Kolla, J.H. Chen, M. Ihme, Assessment of model assumptions and budget terms of the unsteady flamelet equations for a turbulent reacting jet-in-cross-flow, *Combust. Flame* 161 (10) (2014) 2601–2613.